Bioactive Materials 36 (2024) 83–95

Contents lists available at ScienceDirect

Bioactive Materials

journal homepage: www.keaipublishing.com/en/journals/bioactive-materials

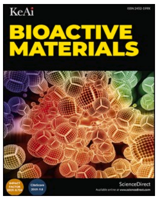

Microneedle-assisted dual delivery of PUMA gene and celastrol for synergistic therapy of rheumatoid arthritis through restoring synovial homeostasis

Peng Hua, Ruifeng Liang, Suleixin Yang, Yanbei Tu, Meiwan Chen *

State Key Laboratory of Quality Research in Chinese Medicine, Institute of Chinese Medical Sciences, University of Macau, Macau SAR, China

ARTICLE INFO

Keywords:
Rheumatoid arthritis
PUMA
Celastrol
Anti-inflammation
Fibroblast-like synoviocyte apoptosis

ABSTRACT

Abnormal proliferation of aggressive fibroblast-like synoviocytes (FLS) and perpetuate synovial inflammation can inevitably accelerate the progression of rheumatoid arthritis (RA). Herein, a strategy of simultaneously promoting FLS apoptosis and inhibiting inflammation as mediated by macrophages is proposed to restore synovial homeostasis for effective RA therapy. A hyaluronic acid-based dissolvable microneedle (MN) is fabricated for transdermal delivery of dual human serum albumin (HSA)-contained biomimetic nanocomplexes to regulate RA FLS and macrophages. Upon skin insertion, dual nanocomplexes are released rapidly from the MN and accumulate in RA joint microenvironment through both passive and active targeting as mediated by HSA. Thioketal-crosslinked fluorinated polyethyleneimine 1.8 K (^{TK}PF) was constructed to bind the plasmid encoding pro-apoptotic gene PUMA with HSA coating layer (^{TK}PF/pPUMA@HSA, TPH). TPH nanocomplexes can upregulate PUMA through RA FLS transfection to trigger efficient apoptosis. Also, HSA nanocomplexes encapsulating the classic anti-inflammatory natural product celastrol (Cel@HSA, CH) can inhibit inflammation of macrophages through blocking NF-κB pathway activation. TPH/CH MN can deplete RA FLS and inhibit M1 macrophage activation, suppress synovial hyperplasia as well as reduce bone and cartilage erosion in a collagen-induced arthritis (CIA) mouse model, demonstrating a promising strategy for efficient RA treatment.

1. Introduction

Rheumatoid arthritis (RA) as a complicated autoimmune disease accompanies with persistent synovial inflammation, progressive cartilage erosion and even complications in other organs [1,2]. The continuous progression of RA ultimately renders non-reversible joint deformity and disability, posing great healthcare and economic burden [3]. Fibroblast-like synoviocytes (FLS) as resident stromal elements play an essential role in RA pathogenesis. The lining layer of FLS in the synovium are markedly expanded from a thickness of 1–3 cell to 10–20 cell and activated with the aggressive phenotype (RA FLS) in disease progression. This property correlates with disease duration, macrophage infiltration as well as the severity of the cartilage and bone damage through producing pathogenic mediators such as inflammatory cytokines, proangiogenic factors, and matrix-degrading enzymes [4,5]. Targeting FLS has been deemed as an effective approach to restoring synovial homeostasis for reversing bone and cartilage destruction [6–9]. Emerging strategies to regulate RA FLS have attained attention *via* changing metabolic profile [10], modulating signal transduction [11] and regulating surface marker [12] to decrease RA FLS invasiveness and disease severity. Considering the uncontrolled proliferation and accumulation of aggressive RA FLS can lead to resistance to cell death signals under oxidative stress in RA microenvironment, overcoming protective signaling to induce effective cell death of RA FLS may represent a practical anti-arthritis treatment. For instance, the expression of pro-apoptotic gene PUMA (p53 upregulated modulator of apoptosis) is low in RA FLS, which partially accounts for the resistance of RA FLS to apoptosis [13]. Delivering proapoptotic gene PUMA *via* viral vectors has been proven to be an effective apoptotic therapy for RA FLS [14,15], but the actual therapeutic efficacy of gene therapy based on viral vectors is restricted by the carcinogenesis, immunogenicity and limited packaging capacity [16–18]. Our group has developed a reactive oxygen species (ROS) responsive polyethylenimine-based fluorinated polymers (^{TK}PF) for the delivery of gene drugs and has been used for cancer therapy [19,

---

Peer review under responsibility of KeAi Communications Co., Ltd.

* Corresponding author.

E-mail address: mwchen@um.edu.mo (M. Chen).

https://doi.org/10.1016/j.bioactmat.2024.02.030
Received 14 December 2023; Received in revised form 17 February 2024; Accepted 23 February 2024

20], which could overcome the limitations of viral vectors and realized enhanced transfection efficiency and decreased cytotoxicity. Thus, developing non-viral gene vectors based on ^{TK}PF with enhanced stability, controlled payload release, and increased transfection capacity to regulate RA FLS is promising for RA gene therapy.

As FLS and macrophages are two core tissue resident cells forming the basis of joint microenvironment to maintain synovial homeostasis, the crosstalk between RA FLS and macrophages is significant in persistent synovial inflammation [21]. The proinflammatory M1 macrophages could stimulate FLS to transform into invasive phenotypes through secreting tumor necrosis factor (TNF) and interleukin-6 (IL-6) [22]. Hence, we hypothesized that inducing efficient apoptosis of RA FLS could be combined with anti-inflammatory drugs for regulating macrophages to enhance anti-arthritic efficacy. Various anti-inflammatory ingredients from traditional Chinese medicine such as celastrol, berberine and sinomenine have revealed great potential as alternative antirheumatic drugs [23,24]. Celastrol has exhibited good therapeutic efficacy and low side effects in RA treatment [25–28]. Cel also could suppress macrophage repolarization toward pro-inflammatory M1 phenotype through regulating NF-κB pathway to decrease inflammatory cytokine secretion [27]. Accordingly, the simultaneous regulation of RA FLS by upregulating PUMA and inhibition of inflammatory responses of macrophages as mediated by Cel may represent a promising therapeutic strategy to reduce synovial inflammation and alleviate bone erosion through restoring synovial homeostasis in advanced RA.

Transdermal delivery systems for RA therapy have received growing attention to overcome the first-pass effect of oral route and increase patient compliance compared with systemic or intra-articular injection [29,30]. Polymeric microneedles (MN) with the advantages of pain-free, non-invasiveness and self-administration has inspired researchers to explore their potential applications in the management of chronic diseases including RA [31]. Moreover, multiple drugs or nanoformulations could be loaded into an MN patch in separated zones or in a mixed manner to achieve an increased convenience and user-friendliness for combined therapy compared with sequential drug injection [32–34]. However, the lack of active targeting ability results in low efficiency for drug delivery to inflamed joints, severely undermining the anti-arthritic effect of therapeutic MN. The recent study unveiled that the highly expressed secreted protein acidic and rich in cysteine (SPARC) in the synovial fluid significantly enhanced the accumulation of human serum albumin (HSA) due to the inherent high affinity for albumin [35]. Therefore, taking advantage of HSA both as the coating layer of the ^{TK}PF-pDNA polyplex and delivery carrier of Cel could prolong circulation and enhance RA targeting ability of the two nanoformulations. Up to now, there have been no reports employing MN patch to regulate RA FLS and macrophages for RA treatment.

Herein, we reported a hyaluronic acid (HA)-fabricated dissolvable microneedle loaded with dual nanomedicine that can induce RA FLS apoptosis and regulate macrophage for alleviating synovial inflammation and bone destruction. Specifically, ^{TK}PF was employed as an efficient gene carrier to bind the plasmid encoding pro-apoptotic gene PUMA, followed by HSA coating to form nanocomplex *via* electrostatic interaction (^{TK}PF/pPUMA@HSA, TPH). Albumin nanocomplex was employed to encapsulate the model anti-inflammatory drug celastrol (Cel@HSA, CH). Dual nanocomplex-loaded HA MN (TPH/CH MN) was strong enough for skin insertion and rapid drug release. The released TPH and CH NCs could accumulate in the RA joint through passive targeting based on ELVIS effect and active targeting due to the high affinity of albumin to SPARC. The disassembled TPH NCs released pPUMA responding to the high ROS level in RA joint and upregulated PUMA to trigger RA FLS apoptosis, which facilitated the restoration of synovial homeostasis in RA. Meanwhile, Cel was released from CH NCs in the slightly acidic environment of macrophage to relieve inflammation for enhanced anti-arthritic outcome. Taken together, the proposed MN-assisted delivery of dual nanomedicine for combined FLS targeted apoptosis and inflammation alleviation is expected to significantly attenuate arthritis progression for effective RA treatment.

2. Materials

2.1. Materials

PEI 1.8 K and heptafluorobutyric anhydride were bought from Aladdin Reagents (Shanghai, China). PEI 25 K and lipopolysaccharide (LPS) was obtained from Sigma-Aldrich (St. Louis, USA). Human serum albumin and celastrol were bought from Macklin Biochemical (Shanghai, China). Hyaluronic acid (90 kDa) was got from Bloomage Freda Co., Ltd. (Shandong, China). The PUMA plasmid was constructed by BGI Genomics Co., Ltd. (Shenzhen, China). Live/dead cell double staining kit and Hoechst 33,342 were obtained from Beyotime Biotechnology (Shanghai, China). Annexin V-FITC/PI apoptosis kit was purchased from Dalian Meilun Biotech Co., Ltd. (Dalian, China). Anti-PUMA primary antibody and secondary antibody were provided by Huabio-Antibodies (Hangzhou, China). ELISA kits were bought from Jiancheng Bioengineering Institute (Nanjing, China). Human TNF-α recombinant protein, Cy5, YOYO-1 and TOTO-3 was bought from Invitrogen (Carlsbad, CA, USA). Bovine type II collagens, incomplete and complete Freund's adjuvant were purchased from Chondrex (Redmond, USA). FLS were got from Jenniobio Biotechnology Co., Ltd. (Guangzhou, China). RAW264.7 cells were obtained from American Type Culture Collection (ATCC, Rockville, USA). RPMI 1640 medium, trypsin EDTA, fetal bovine serum (FBS), and PBS were obtained from Gibco (Life Technologies, Grand Island, NY, USA).

2.2. Preparation and characterization of TPH and CH NCs

^{TK}PF was synthesized as our group previously reported [19,20]. To prepare binary ^{TK}PF/pDNA NCs, pDNA (250 μg/mL) was mixed with ^{TK}PF (5 mg/mL) at a mass ratio of 10:1 and incubated for a duration of 30 min. HSA dissolved in PBS (5 mg/mL) was added to ^{TK}PF/pDNA NCs at various HSA/^{TK}PF weight ratios from 1:10 to 7:10 for 30 min to form TPH NCs. ^{TK}PF/pPUMA NCs at different weight ratios of ^{TK}PF and pPUMA were conducted in 1% agarose electrophoresis with 150 V for a duration of 15 min to evaluate the nucleic acid condensation ability, which were further visualized by the gel-doc system (ChemiDoc MP, Bio-Rad, USA) after the electrophoresis ended. CH NCs were fabricated as the previously described method with some modification [36,37]. Briefly, 100 μL of Cel dissolved in DMSO (10 mg/mL) was added dropwise slowly to the 2 mL of HSA dissolved in PBS solution (5 mg/mL). The mixture was stirred overnight and then transferred into dialysis bags (MWCO 3500) in order to remove DMSO, free Cel and excess HSA. Dir-loaded HSA nanocomplexes were prepared as the similar method. The particle size and zeta potential of ^{TK}PF/pPUMA, TPH and CH NCs was measured by DLS (Nano-ZS Zetasizer instrument, Malvern, UK). Additionally, their morphology was observed *via* transmission electron microscopy (TEM, Ht-7800, Hitachi, Japan). The encapsulation efficiency and loading capacity of CH NCs were assessed by HPLC (Waters, Milford, MA) and calculated as the previously reported method [38]. The UV–vis absorbance spectrum of HSA, Cel, and HSA NCs was measured by the GENESYS™ 150 UV–Vis–NIR spectrometer (Thermo Fisher, USA). To evaluate the *in vitro* drug release behavior, CH NCs were transferred into a dialysis bag in PBS containing 5% Tween-80 at pH 5.8 or 7.4. The solution (1 mL) was collected, and another fresh buffer was supplemented at the predetermined time. The released Cel was quantified by HPLC.

2.3. Cellular uptake assay

FLS were seeded into 24-well plates and permitted to incubate overnight. The culture medium was then replaced, and 10 ng/mL of recombinant human TNF-α was added for stimulation for a period of 4 h. YOYO-1 labeled plasmids were fabricated according to the manufacturer's instruction for further construction of ^{TK}PF/pDNA and TPH NCs. The complexes in serum-free medium were added to the well. After incubation for 0.5, 1, 2, 4 h, the cells were visualized by DMI8 inverted fluorescent microscope, and were harvested for analysis by flow cytometry (FCM, Cytoflex, Beckman, USA). RAW264.7 cells were cultured overnight and stimulated with or without LPS (1 μg/mL) for 24 h. FITC labeled CH NCs were added and cultured for 1, 2, 4 h. Cells were subsequently collected for FCM analysis.

2.4. *Endosomal escape of TPH NCs*

TPH NCs containing Cy-5-labeled pDNA were prepared according to the above-mentioned method. FLS were seeded into 35 mm confocal dishes, cultured for 24 h and stimulated by TNF-α. Then FLS were incubated with TPH NCs at the time intervals of 1, 2, 4, and 8 h. LysoTracker green and Hoechst 33342 were used to stain the lyso/endosomes and nuclei, respectively. After being washed and fixed with 4% paraformaldehyde for 15 min, FLS were observed by confocal laser scanning microscopy (CLSM, Leica TCS SP8, Germany).

2.5. *Transfection efficiency of TPH NCs in vitro*

FLS were cultured in the 12-well plate, incubated overnight and then stimulated by TNF-α prior to transfection. ^{TK}PF/pDNA and TPH NCs containing 1 μg of pEGFP (≈5 Kb) were added into each well with serum-free RPMI 1640 medium for 6 h incubation. Then the medium was substituted with fresh complete medium and incubated for 24 h. The EGFP expression was observed by DMI8 inverted fluorescent microscope (Leica, Germany) and quantified by FCM analysis.

2.6. *Cell proliferation assay*

FLS were cultured in 96-well plates (5×10^3 cells per well) and activated with TNF-α for 4 h. TPH NCs containing 0.1 μg pPUMA was added to the well with serum-free medium. Upon a 6-h incubation, the medium was replaced with a complete medium and the FLS were cultured for an additional 24 h. Similarly, RAW264.7 were cultured overnight and treated with CH NCs at various concentrations for 24 h. The inhibition of cell proliferation treated by TPH NCs, and the cell cytotoxicity of CH NCs were evaluated by MTT assay.

2.7. *Live/dead staining*

FLS were cultured in 12-well plates at a density of 5×10^5 cells/well overnight and stimulated by TNF-α. Cells were then incubated with TPH NCs (1 μg pPUMA) for 6 h, followed by replacing fresh medium for another 24 h of incubation. After being stained by calcein-AM and propidium iodide (PI) for 15 min, FLS were captured by fluorescent microscope.

2.8. *Cell apoptosis analysis*

FLS were cultured in 6-well plates (3.0×10^5 cells/well) with the stimulation of TNF-α for 24 h. Cells were treated by TPH NCs in fresh serum-free medium (2 μg pPUMA) for 6 h, and then incubated with fresh medium for 24 h. To evaluate the pro-apoptosis effect of TPH NCs *in vitro*, Annexin V-FITC/PI staining were performed for analysis by FCM.

2.9. *Western blotting*

To evaluate the change of PUMA protein after TPH transfection, Western blot analysis was conducted. The cells were rinsed, lysed and collected *via* centrifugation at 10,000×g for 10 min. The total protein content of each group was quantified through BCA assay. Subsequently, proteins were separated by 12% SDS-PAGE and transferred onto PVDF membrane electronically. After being blocked in TBST buffer containing 5% BSA, the membrane was incubated with primary antibody overnight at 4 °C and secondary antibody for a duration of 1 h at room temperature. Finally, the membrane was visualized *via* Clarity Western ECL substrate and exposed by gel-doc system (ChemiDoc MP, Bio-Rad, USA). In addition, RAW264.7 cells were stimulated with LPS and treated with CH NCs. The changes of p65, p-p65, IκBα, pIκBα were also evaluated using Western Blotting as the procedures mentioned above.

2.10. *Macrophage repolarization*

RAW264.7 cells were seeded in 24-well plates and allowed to culture overnight. The LPS was added in the concentration of 1 μg/mL for a 24-h incubation period, followed by the addition of CH NCs at a dosage of 500 ng/mL for 12 h. After incubation, CD16/32 was added for a 10-min duration to block Fc-receptors. Subsequently, the cells were stained with FITC conjugated anti-CD86 antibody, and APC conjugated anti- CD206 antibody for 30 min and subsequently analyzed using FCM.

2.11. *Preparation and characterization of TPH/CH MN*

The TPH/CH MN was fabricated through the reported micromolding method [39]. Briefly, the constructed TPH and CH NCs were mixed and added in HA aqueous solution (200 mg/mL). The mixture was poured in the PDMS mold and then centrifuged at the speed of 3000 rpm for 30 min to allow TPH and CH NCs fully deposited in the cavities of needles. The excessive solution was removed and 600 μl of blank HA solution was added to the mold for further centrifugation at 3000 rpm for 30 min, which was dried overnight at room temperature. TPH/CH MN was obtained through detachment from the mold. HA MN that encapsulating YoYo-1 labeled TPH NCs and DiR-labeled HSA NCs were fabricated through the same method. The morphology of TPH/CH MN was characterized by SEM and fluorescence microscope. The mechanical strength of TPH/CH MN was assessed through a texture analyzer (TMS-PRO, FTC, VA, USA).

2.12. *CIA mouse model*

DBA-1J male mice (6–8 weeks old) were procured from Gempharmatech Co., Ltd (Jiangsu, China). The CIA model was established through double immunization as the literature reported [40,41]. An immunization grade bovine type-II collagen solution (2 mg/mL) and complete Freund's adjuvant solution (4 mg/mL) were mixed by a homogenizer in an ice bath. For the first immunization, mice were intradermally injected with an emulsion of the mixture at the end of the tail. On Day 21, boost immunization was performed by injecting the mixed emulsion of type-II collagen and incomplete Freund's adjuvant. All animals were housed in pathogen-free conditions and subjected to standard 12-h light/12-h dark periods, with access to sufficient food and water. All animal experiments were conducted in accordance with the regulations approved by the Animal Care and Use Committee of Zunyi Medical University (Zhuhai campus, permit no. ZHSC-2-2023-043).

2.13. *In vivo therapy protocol*

The study randomly assigned the mice into six groups as follows ($n = 6$): Normal, model (saline-treated), TPH/CH NCs (20 μg pPUMA, 100 μg Cel), TPH MN (20 μg pPUMA), CH MN (100 μg Cel) and TPH/CH MN (20 μg pPUMA, 100 μg Cel) group. After 28 days of the first immunization, TPH MN, CH MN and TPH/CH MN were topically applied in the back skin every three days for 7 times. The right hind paw thickness of e was quantified every 3 days by a vernier caliper and the clinical score sum of four limbs were recorded according to the scoring criteria [41].

2.14. *Micro-CT analysis*

At day 49, posterior limbs were imaged using a computed tomography scanner (nanoScan PET/CT 82s, Mediso, Hungarian) under 50-kV and 1-mA x-ray beam. The reconstructed three-dimensional images were obtained from the micro-CT data set and processed *via* RadiAnt DICOM Viewer (Version 2022.1, Medixant, Poland).

2.15. *In vivo serum cytokine evaluation*

The mice were euthanized after micro-CT imaging at day 49 to collect the blood samples. The samples were clotted at 37 °C for 30 min and then centrifugated at a speed of 3000×*g* for 15 min. The collected supernatant serum was measured to reveal the level of TNF-α, IL6 and IL-1β as guided by the instructions of the ELISA kits.

2.16. *Histological analysis*

The mice were euthanized at the endpoint of study to collect the hind ankle joints. These joints were fixed in a 4% paraformaldehyde solution, followed by decalcification using a 15% (w/v) tetrasodium ethylenediaminetetraacetic acid solution for three weeks. After being embedded in paraffin, the decalcified joints were subsequently sectioned for H&E, safranin-O and toluidine blue (T&B) staining. Immunohistochemistry was performed for PUMA staining to verify the *in vivo* transfection of TPH, and for CD68 and CD90 staining to investigate the abundance change of macrophage and RA FLS. The sectioned tissues were visualized under an DMI8 inverted microscope (Leica, Germany).

2.17. *Biocompatibility analysis*

The major organs of the mice were collected and fixed using a 4% (w/v) paraformaldehyde solution, followed by embedding the organs in paraffin. Slices of 3-μm thickness were obtained from the organs for H&E staining, and images of these slices were obtained using an Olympus microscope (Tokyo, Japan).

2.18. *Statistical analysis*

All quantitative data were reported as mean with standard deviation (mean ± SD). For statistical analysis, Student's two-tail *t*-test was applied for two-group comparisons while one-way analysis of variance (ANOVA) was utilized to analyze data involving multiple comparisons. A significance level of $p < 0.05$ was considered statistically significant.

3. Results and discussion

3.1. *Fabrication and characterization of TPH and CH NCs*

The fabrication process of TPH and CH nanocomplex is illustrated in Scheme 1. For the construction of TPH nanocomplex, ROS-responsive polyethylenimine-based fluorinated polymers (^{TK}PF) was first

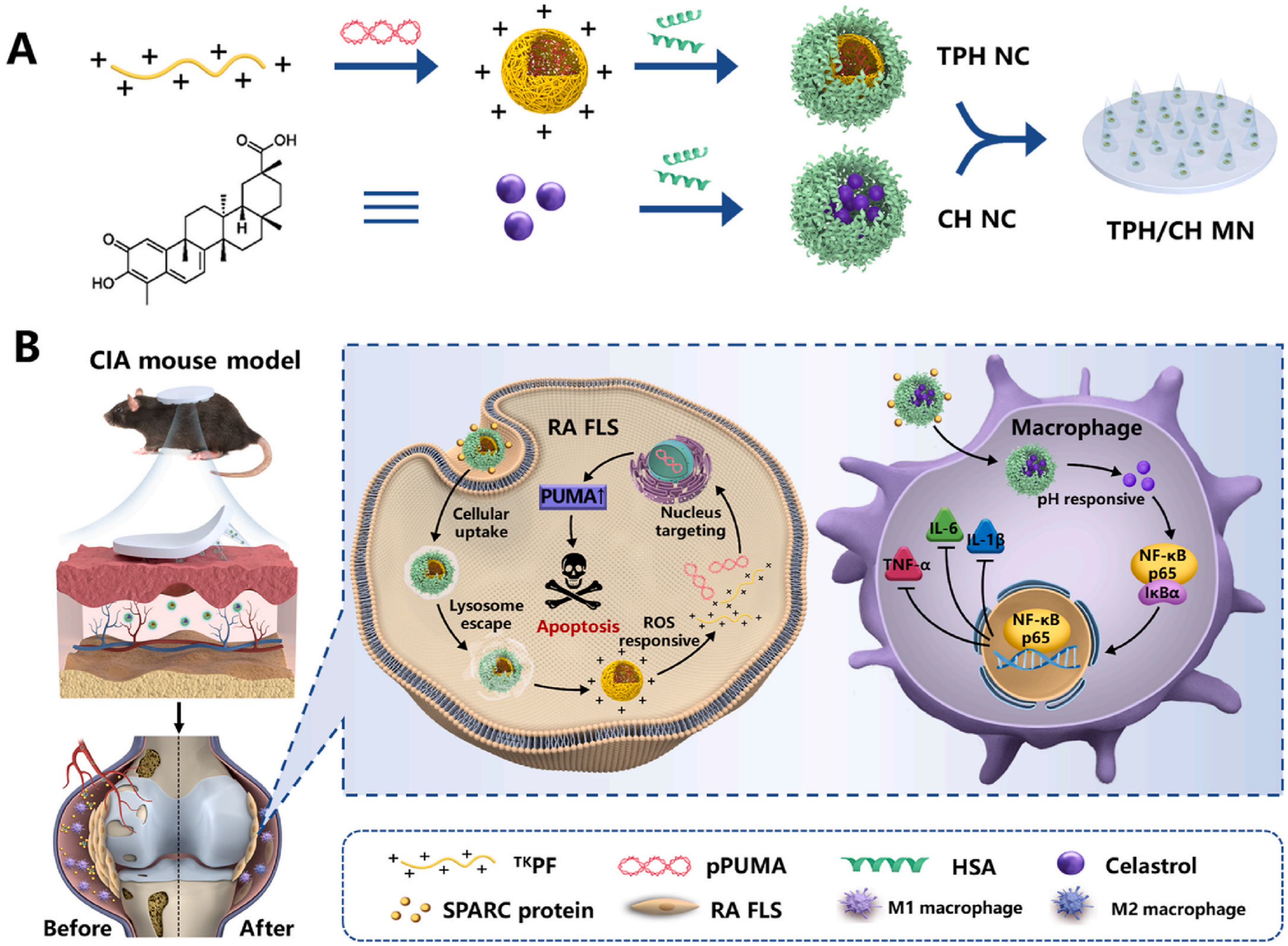

Scheme 1. Schematic illustration of (A) the fabrication procedures of the HA-based microneedle encapsulated with dual HSA-contained nanocomplexes (TPH/CH MN) and (B) the RA therapeutic mechanism through inducing RA FLS apoptosis and regulating inflammatory macrophages.

synthesized by crosslinking PEI 1.8 K with the thioketal linker, followed by the modification of heptafluorobutyric anhydride to obtain the thioketal-crosslinked fluorinated polyethyleneimine as our previous work reported [19,20]. The binary nanocomplex was obtained *via* electrostatic interactions by mixing the cationic polymer ^{TK}PF and negatively charged PUMA plasmid at the ratio of 10:1, which showed a particle size of 168 ± 4 nm with polydispersity index (PDI) of 0.26 ± 0.02) and a positive zeta potential of +33.1 ± 1.2 mV (Fig. 1A). The negatively charged human serum albumin (HSA) was then coated on the surface of ^{TK}PF/pPUMA NCs through electrostatic attraction [42,43]. The change of size distribution and zeta potential was investigated after mixing different amount of HSA with ^{TK}PF/pPUMA at different weight ratios between HSA and ^{TK}PF from 1:10 to 7:10. The zeta potential of ^{TK}PF/pPUMA@HSA NCs dropped gradually from positive to negative with HSA adding incrementally (Fig. S1). TPH NCs at the weight ratio of 5:10 exhibited uniform size (204 nm, PDI 0.269) and slightly positive charged (1.6 mV), which was screened as the optimal ratio for further experiments (Fig. 1E). The obtained TPH NCs still revealed spherical-like morphology under transmission electron microscope (TEM) (Fig. 1B). ^{TK}PF exhibited excellent pDNA condense ability as shown in the gel retardation assay (Fig. 1F). The migration of pDNA could be totally retarded in ^{TK}PF/pDNA at a low mass ratio of 1:1 (^{TK}PF: pDNA). Moreover, the coating of HSA onto ^{TK}PF/pPUMA NCs did not result in the plasmid leakage (Fig. 1F). In addition, TPH NCs was stored at 4 °C with uniform and stable size for 1 week (Fig. S2). Cel was encapsulated within the HSA hydrophobic pocket *via* hydrophobic interactions to obtain CH NCs according to the method our previous study reported [37]. According to dynamic light scattering (DLS) data, CH NCs were well dispersed in phosphate-buffered saline (PBS) (PDI 0.22 ± 0.03) with the average hydrodynamic diameter of 135.4 ± 2.1 nm and the zeta potential of −27.1 ± 1.8 mV (Fig. 1C). The TEM image of CH NCs revealed common spherical structures (Fig. 1D). The encapsulation efficiency and loading capacity of Cel in CH NCs was determined as 80.6 % and 7.33 %, respectively. The successful encapsulation of Cel in the HSA nanocomplex was further confirmed by UV–vis–NIR spectra in Fig. 1G, where free Cel and CH NCs showed a strong absorbance at around 430 nm. The long-term stability of CH NCs was assessed by monitoring the hydrodynamic size in PBS for a week with almost no change (Fig. S3). Locally decreased environmental pH is characteristic for many chronic inflammatory diseases such as atherosclerosis and RA [44,45]. The pH responsive drug release behavior of CH NCs was then investigated. The release percentage of Cel from CH NCs was only 36.3 ± 3.4% in neutral condition while Cel was released rapidly for 52.7 ± 1.5% in acidic environment after 48 h, demonstrating CH NCs easy to release payloads in M1 macrophages (Fig. 1H).

3.2. Characterization of TPH/CH@MN

Microneedle as a non-invasive transdermal delivery tool can enhance drug penetration through generating micropores of skin, showing convenience and comfort compared with intravenous injection and intra-articular injection for RA therapy. The dissolvable TPH/CH@MN patch was fabricated using biocompatible hyaluronic acid (HA) *via* a micromolding approach [39]. The TPH/CH@HA MN patch was 6 mm in diameter contained 136 needle tips. MN tip exhibited conical shape, possessing a base diameter of 400 μm and a height of 600 μm as shown in the SEM image (Fig. 1I). To effectively pierce the skin for drug transdermal delivery, microneedle tips should possess sufficient mechanical strength. The force-displacement curve of TPH/CH@MN didn't exhibit obvious change compared with blank MN, indicating that the

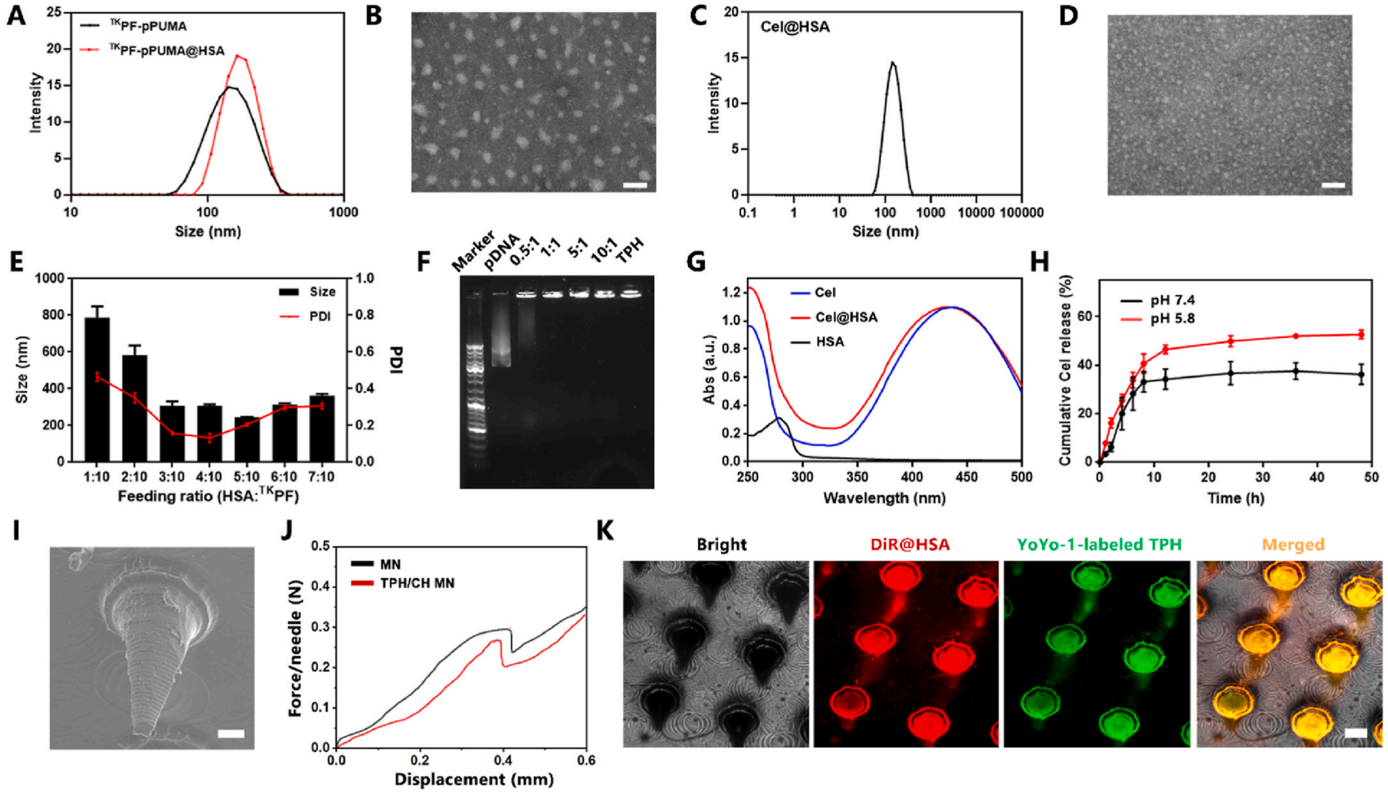

Fig. 1. Characterization of TPH NCs, CH NCs and TPH/CH MN. (A) DLS analysis of ^{TK}PF/pPUMA and TPH NCs. (B) Morphology of TPH NCs capture by TEM. Scale bar, 100 nm. (C) Particle size of CH NCs. (D) Morphology of CH NCs capture by TEM. Scale bar, 100 nm. (E) Size and PDI of TPH NCs with different ratios of HSA and ^{TK}PF. Data represent mean ± SD ($n = 3$ independent samples). (F) Agarose gel electrophoresis of ^{TK}PF/pPUMA at various ^{TK}PF/pPUMA weight ratios and TPH NCs. (G) UV–vis absorbance spectra of Cel (0.1 mg/mL), HSA (0.5 mg/mL), and CH NCs. (H) *In vitro* release profile of Cel from CH NCs. (I) SEM image of TPH/CH MN. Scale bar, 100 μm. Data represent mean ± SD ($n = 3$). (J) Mechanical strength characterization of the HA-fabricated MN and TPH/CH loaded HA MN patch. (K) Fluorescence images of MN containing YoYo-1 labeled TPH NCs and DiR-labeled HSA NCs. Scale bar, 200 μm.

encapsulation of dual nanocomplexes did not significantly influence the mechanical strength of MN (Fig. 1J). The fracture forces of the blank MN and TPH/CH@MN were quantitatively measured as 0.30 and 0.26 N per needle, both of which surpass 0.1 N, the reported minimum skin insertion force [46]. As shown in Fig. 1K, dual fluorescence was observed in the fluorescence images of the MN patch containing YoYo-1-labeled TPH NCs and DiR-labeled CH NCs, indicating the uniform distribution of TPH and CH NCs in the MN tips. The results confirmed the successful fabrication of MN patch to encapsulate both TPH and CH NCs. The *in vitro* skin insertion capacity was further evaluated through applying MN to pierce excised porcine skin. The Rhodamine B-loaded MN was pressed against porcine skin for 10 min and then withdrawn. The red fluorescent spots were observed by fluorescence microscope (Fig. S4). To further visualize the penetration depth, Rhodamine B-loaded MN was applied in mouse skin for 10 min to observe the red fluorescence signal at different depths. The constructed HA-based MN could pierce the skin with a penetration depth of around 270 μm (Fig. S5), indicating the fabricated MN could successfully inserted into the skin.

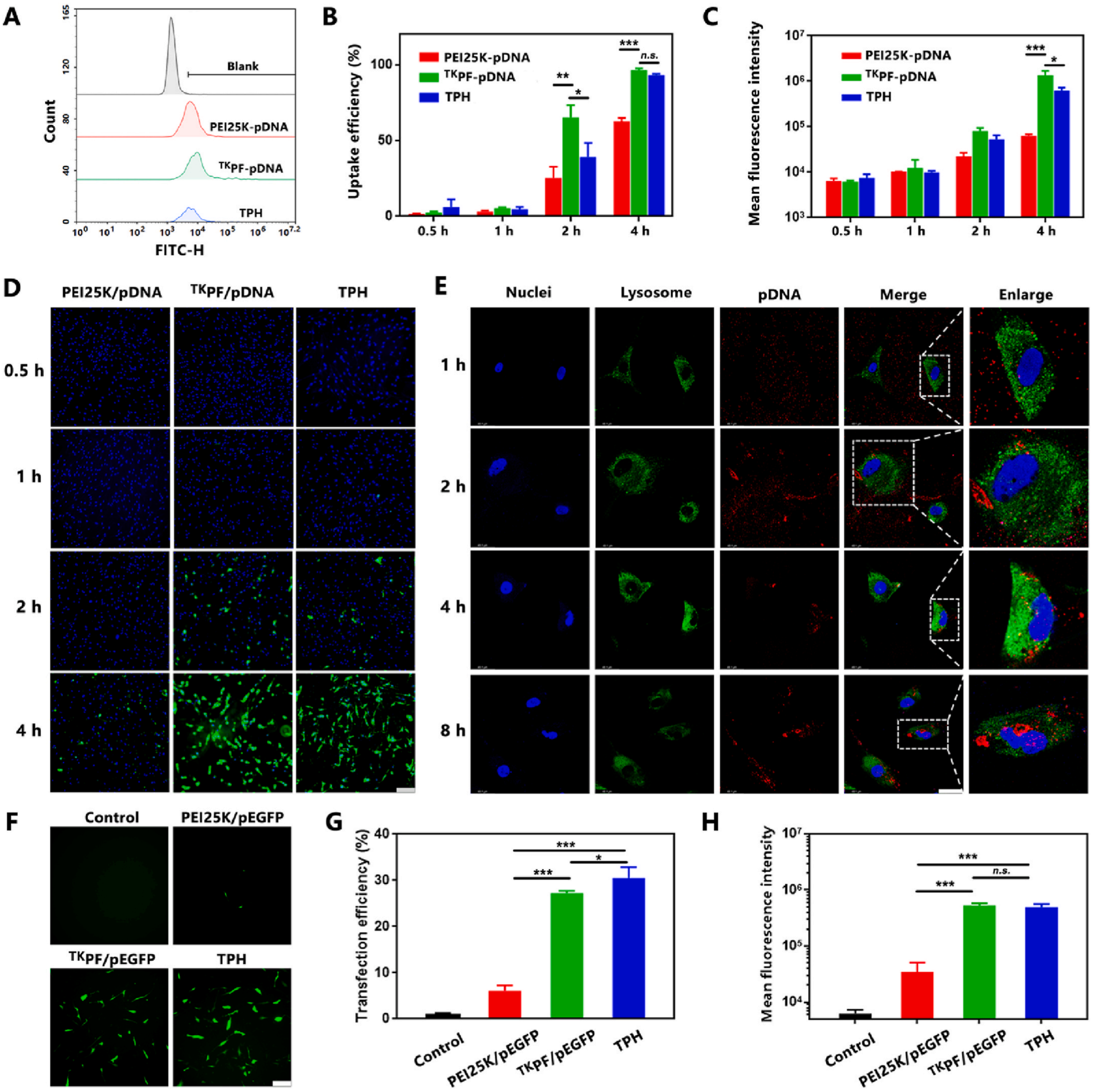

Fig. 2. Characterization of cellular uptake, endosome escape, and transfection efficiency of TPH NCs. (A) Cellular uptake of RA FLS treated YOYO-1 labeled PEI25 K/pDNA, ^{TK}PF/pDNA and TPH NCs by Flow cytometry analysis. (B) Quantitative cellular uptake efficiency and (C) mean fluorescence intensity of PEI25 K/pDNA, ^{TK}PF/pDNA, and TPH detected by flow cytometry. (D) Fluorescence microscopy images of RA FLS after incubation with PEI25 K/pDNA, ^{TK}PF/pDNA, and TPH. Scale bar: 200 μm. (E) CLSM images of RA FLS incubated with TPH NCs. Scale bar: 50 μm. (F) Fluorescence images of RA FLS treated by PEI25 K/pDNA, ^{TK}PF/pDNA and TPH NCs using pEGFP after transfection for 24 h. Scale bar: 200 μm. (G) Quantitative transfection efficiency result analyzed through flow cytometry. (H) Mean fluorescence intensity by flow cytometry. Data are shown as mean ± SD (n = 3). $^{*}p < 0.05$, $^{**}p < 0.01$, $^{***}p < 0.001$.

3.3. Cellular uptake and endosomal escape of TPH NCs in RA FLS

The cellular uptake efficiency of TPH NCs was investigated in TNF-α-activated FLS by flow cytometric analysis. TNF-α was used to trigger abnormal proliferation of FLS and to induce the invasive phenotype of RA FLS [47,48]. As revealed by the uptake efficiency and mean fluorescence intensity (MFI) in Fig. 2A–D, YOYO-1 labeled $^{\text{TK}}$PF/pDNA and TPH NCs both showed enhanced cellar internalization than PEI 25 K/pDNA at 2 h and 4 h, which could be attributed to the fluorination strategy endowing the cationic polymer with both hydrophobic and lipophobic features to improve the cellular uptake efficiency [20,49,50]. To be noted, TPH NCs with much lower positive charge than $^{\text{TK}}$PF/pDNA showed similar cellular internalization (93.3 ± 0.7%) to $^{\text{TK}}$PF/pDNA (96.4 ± 1.1%), which was significantly higher than PEI 25 K/pDNA (62.7 ± 1.9%) in RA FLS (Fig. 2B). It could be attributed to the specific targeting of HSA to SPARC protein overexpressed in activated macrophage and FLS [51]. After endocytosis, effective lyso/endosomal escape is the prerequisite for successful transfection [52]. The endosomal escape capability of TPH NCs was investigated on RA FLS by confocal scanning laser microscope (CLSM, Fig. 2E). TPH NCs loaded with Cy5-labeled pDNA (red) mainly localized in cell membranes, which was not effectively endocytosed after 1 h incubation. At 2 h, TPH NCs were taken up and localized in green-stained lysosomes. Subsequently, the internalized TPH NCs gradually escaped from endosomes at 4 h. After incubation for 8 h, Cy5-labeled pDNA of TPH NCs eventually accumulated into the nucleus. These results confirmed the effective lysosome escape and nucleus targeting capacity of TPH NCs.

3.4. Transfection efficiency of TPH NCs in RA FLS

Cytotoxicity is a crucial issue for the gene delivery systems. We evaluated the cytotoxicity of $^{\text{TK}}$PF in both NIH/3T3 and RA FLS using MTT assay (Fig. S6). $^{\text{TK}}$PF showed negligible cytotoxicity, which could be attributed to the ROS-sensitive thioketal linkages leading to the reduction of the molecular weight [53]. The transfection of TPH NCs was evaluated on RA FLS in comparison with PEI25K polyplexes at the mass ratio of 2:1, which is the gold standard of non-viral vectors. The plasmid encoding enhanced green fluioresce protein (EGFP) as a reporter gene was utilized. The transfection efficiency of $^{\text{TK}}$PF/pDNA polyplexes (27.2 %) was much higher than that of the control PEI 25 K/pDNA (6.0 %) in TNF-α-treated RA FLS (Fig. 2F). HSA coating slightly enhance the transfection capacity of TPH NCs, which could be attributed to caveolin-dependent endocytosis that HSA entered cells through to bypass the fusion of lysosomes [54,55]. These comparisons demonstrated that $^{\text{TK}}$PF/pDNA and TPH NCs polyplexes were both efficient in transfecting RA FLS (Fig. 2G and H).

3.5. RA FLS apoptosis evaluation of TPH NCs

As demonstrated above, TPH can upregulate p53 up-regulated modulator of apoptosis (PUMA) by transfection to induce apoptosis of RA FLS. Furthermore, we first investigated the anti-proliferation effect of TPH in RA FLS. In Fig. 3A, $^{\text{TK}}$PF/pPUMA showed decreased cell viability (63.3 ± 2.3%) while TPH triggered higher killing effect of RA FLS (48.1 ± 3.6%) ($p < 0.001$), which may be attributed to the enhanced

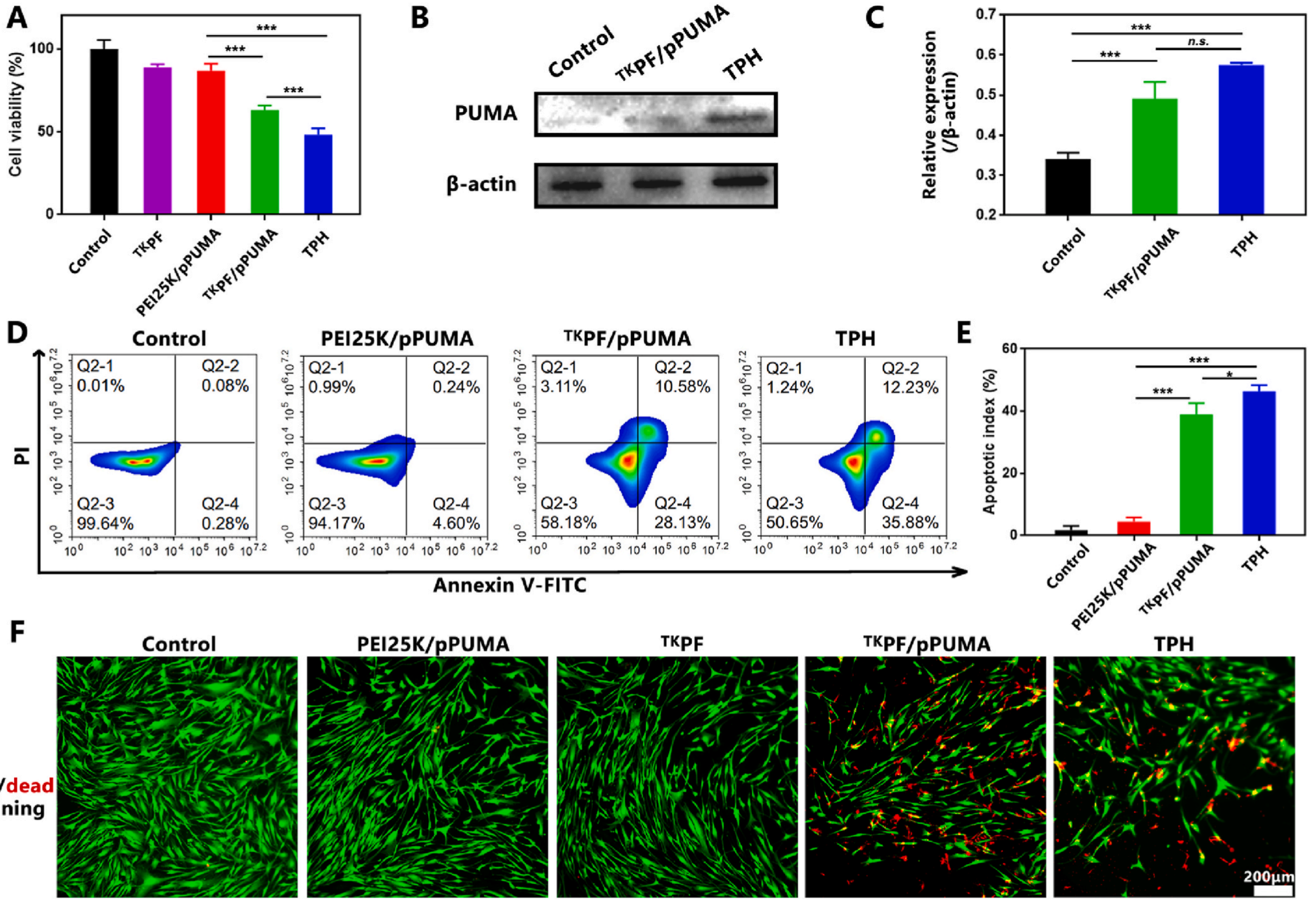

Fig. 3. Evaluation of RA FLS apoptosis of TPH. (A) The cellular viability of RA FLS after being treated by PEI25 K/pPUMA, $^{\text{TK}}$PF/pPUMA and TPH NCs. (B) and (C) PUMA expression detected by Western blot assay. (D) Annexin V-FITC/PI staining of RA FLS treated by PEI25 K/pPUMA, $^{\text{TK}}$PF/pPUMA and TPH NCs analyzed by Flow cytometry and (E) the quantitative result of apoptotic cell percentage in different treatment groups. (F) Fluorescence images of RA FLS double stained by FDA and PI. Data are presented as mean ± SD (n = 3). $^{*}p < 0.05$, $^{**}p < 0.01$, $^{***}p < 0.001$.

transfection capacity of TPH NCs. The mechanism to clarify the apoptosis effect of TPH was investigated by Western blot assays. The result displayed a significant increase in PUMA expression in both the ^{TK}PF/pPUMA and TPH groups in comparison to the blank sample (Fig. 3B and C). Moreover, the apoptotic effect on RA FLS was investigated through Annexin V-FITC/PI staining using flow cytometry (Fig. 3D and E). As expected, RA FLS treated with ^{TK}PF/pPUMA demonstrated a significant increase in apoptosis (39.0 ± 3.0%) and TPH induced higher apoptosis efficiency (46.4 ± 1.6%). Live/dead staining result further confirmed the RA FLS killing effect consistent with the cytotoxicity effect (Fig. 3F). These results indicated the excellent ability of gene vector ^{TK}PF plasmid vector to express the proapoptotic gene PUMA in inducing RA FLS apoptosis.

3.6. Cytotoxicity and cellular uptake of CH NCs in macrophages

Lipopolysaccharide (LPS)-stimulated RAW264.7 macrophages were utilized as the inflammatory cell model to evaluate the anti-inflammatory effect of CH NCs. The viability of RAW264.7 cells incubated with CH NCs were measured through MTT assay. As shown in Fig. 4A, no significant toxicity of CH NCs was observed at investigated doses ranging from 25 to 500 ng/mL. In addition, CH NCs showed no cytotoxicity to RA FLS at the investigated concentrations (Fig. S7). The cellular uptake efficiency of FITC-labeled CH NCs was investigated *via* flow cytometry analysis (Fig. 4B). More efficient cellular uptake of CH NCs was observed in LPS-activated macrophages than macrophages without LPS activation (Fig. 4C), which could be attributed to the increased demand of inflammatory macrophages for albumin [35]. After endocytosis, the acidic microenvironment resulted from excessive lactate generation and anaerobic glycolysis due to the highly metabolic pattern was adventurous for pH responsive Cel release to exert anti-inflammatory effect.

3.7. Anti-inflammatory efficacy of CH NCs in LPS-stimulated macrophages

Cel has been reported to suppress inflammation through inhibiting NF-κB signaling pathway [27,56]. The changes of essential proteins (p65, pp65, IκBα, pIκBα) involved in NF-κB signaling pathway after CH NCs treatment were evaluated by Western blot analysis. Upon LPS stimulation, IκBα and p65 of macrophages were significantly activated. However, CH NCs could obviously lower the phosphorylation of p65 and IκBα, indicating the activation of the NF-κB pathway was significantly inhibited by CH NCs (Fig. 4D). ELISA results also revealed the anti-inflammatory effect of CH to decrease the levels of TNF-α, IL-6 and IL-1β, which were significantly elevated after LPS stimulation (Fig. S8). Then the effects of CH NCs on macrophage polarization were investigated by flow cytometry analysis. As shown in Fig. 4E and F, LPS stimulation significantly increased the proportions of macrophages expressing pro-inflammatory M1-phenotype marker CD86 and decreased those expressing anti-inflammatory M2-phenotype marker CD206. In contrast, CH NCs treatment with resulted in a notable reduction in CD86-labeled M1 phenotype macrophages and a significant increase in CD206-labeled M2 phenotype macrophages in comparison to the LPS group. CH NCs obviously reduced the percentage of CD86-positive M1 macrophages from 33.5% to 9.7% while increased CD206-positive M2 macrophage proportion from 2.4% to 42.4% compared with the LPS-treated group (Fig. 4G and H), demonstrating efficient M1-to-M2 transition induced by CH NCs.

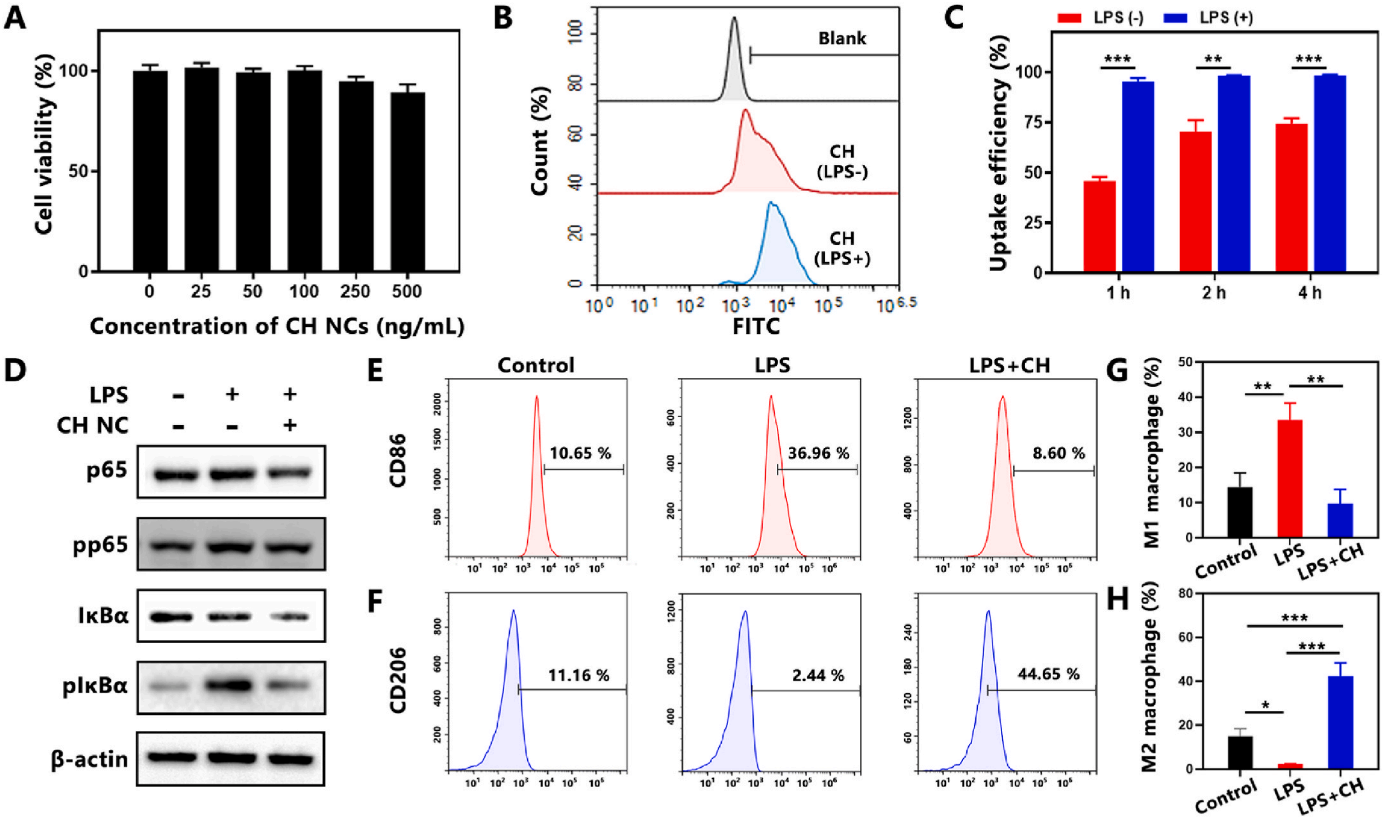

Fig. 4. Cellular uptake and anti-inflammatory evaluation of CH NCs in LPS-induced RAW264.7 macrophages. (A) Cell viability of RAW 264.7 cells treated by CH NCs under various concentrations of Cel. (B) Cellular uptake of FITC-labeled CH NCs in RAW264.7 cells at 4 h analyzed by flow cytometry. (C) Cellular uptake efficiency of FITC-labeled CH NCs detected by flow cytometry at different time. (D) Protein expression of p65, pp65, IκBα and pIκBα measured by western blotting. (E) The percentages of CD86-positive and (F) CD206-positive macrophages after CH NCs treatment evaluated by flow cytometry. (G) Quantitative analysis of M1 and (H) M2 polarization after CH NCs treatment. Data are presented as mean ± SD (n = 3). $^{*}p < 0.05$, $^{**}p < 0.01$, $^{***}p < 0.001$.

3.8. In vivo biodistribution of TPH/CH MN

DBA/1 J mice was utilized to establish the collagen-induced arthritis (CIA) mouse model, following previously documented methods [47]. Subsequently, the *in vivo* fluorescence imaging employing TOTO-3 labeled TPH/CH MN was performed to evaluate the biodistribution of payloads. As shown in Fig. 5A, TOTO-3 labeled TPH NCs were rapidly accumulated in the inflamed joints of CIA mice 3 h post MN application. Conversely, the fluorescence signals observed in the paws of non-arthritic mice was notably weaker than those in CIA mice at both 3 and 6 h. Major organs and paws from normal and CIA mice were collected 6 h post MN application for *ex vivo* fluorescence imaging. Quantification of the fluorescence intensity not only further confirmed the more intraarticular accumulation in inflamed joints than normal joints, but also revealed more accumulation of TPH NCs in paws than major organs (Fig. 5B and C). These results indicated that the payloads released from TPH/CH MN could efficiently accumulate intraarticularly *in situ*. Although a higher fluorescence in the liver was observed in CIA mice than that in normal mice, negligible tissue damage or inflammatory lesions was found (Fig. S9), which was partially attributed to the rapid elimination of nanoparticles by the liver [57].

3.9. TPH/CH MN ameliorated arthritic progression in CIA mice

In order to assess the therapeutic effect of TPH/CH MN in the treatment of RA, the MN were applied topically in an CIA mouse model as the treatment regimen outlined in Fig. 6A. DBA-1J mice were subcutaneously injected with saline, TPH/CH NCs, applied topically with TPH MN, CH MN and TPH/CH MN every three days for 7 times to examine the therapeutic efficacy. No significant alterations in body weight were observed during the treatment period, suggesting the safety profile of TPH/CH MN (Fig. 6C). H&E-stained histological changes of major organs including heart, liver, spleen, lung, and kidney were observed after different treatments to further investigate the potential toxicity. All the major organs did not exhibit any distinct histological changes as compared to the saline group, indicating the biocompatibility of TPH/CH MN (Fig. S9). The severity degree of arthritis could be reflected by paw thickness and clinical scores. Significant increases in hind paw and ankle thickness could be observed in the CIA mice compared with healthy mice (Fig. 6B and D). The TPH MN and CH MN could partially decrease the swelling paw thickness by 49.2% and 40.5%, respectively. By comparison, CIA mice treated by TPH/CH NCs and TPH/CH MN significantly lowered the swelling paw thickness by 67.9% and 74.6%, indicating the excellent therapeutic effect in reducing articular inflammation. The similar therapeutic efficacy of TPH/CH NCs and TPH/CH MN also demonstrated the effectiveness of MN as transdermal drug route. The same trend was also observed in the clinic scoring data (Fig. 6E). TPH MN and CH MN group showed moderate anti-arthritic efficacy of lowering the clinical scores while TPH/CH MN exhibited the lowest clinical scores. Considering bone erosion is a crucial symptom of severe RA, the micro-computed tomography (micro-CT) was employed to investigate the impact of TPH/CH MN on bone erosion in inflamed ankle joints for RA treatment (Fig. 6F). Compared with normal mice, the articular surfaces of toes and ankles of saline-treated CIA mice revealed rough bone surfaces and distinct bone erosion. TPH MN and CH MN group showed moderate therapeutic efficacy against bone destruction in CIA mice. Notably, neglectable bone erosion was observed in the combined treatment (TPH/CH NCs and TPH/CH MN group), which implied inducing RA FLS apoptosis plus relieving inflammation could effectively protect the bones from destruction and erosion.

3.10. TPH/CH MN improved the arthritic inflammation and cartilage damage by FLS depletion and inhibition of macrophages

Bone and cartilage damage are the main features of RA, which can be aggravated and sustained by proliferating synovial tissue. Therefore, histological analysis of arthritic inflammation and cartilage destruction was performed on the ankle joints of CIA mice from different groups to further confirm the therapeutic efficacy of TPH/CH MN. In contrast to healthy mice, CIA mice in saline group demonstrated clear indications of synovial hyperplasia, inflammatory cell infiltration and pannus invasion, as revealed by the H&E-stained results (Fig. 7A). CH MN and TPH MN group partially inhibited both synovial hyperplasia and

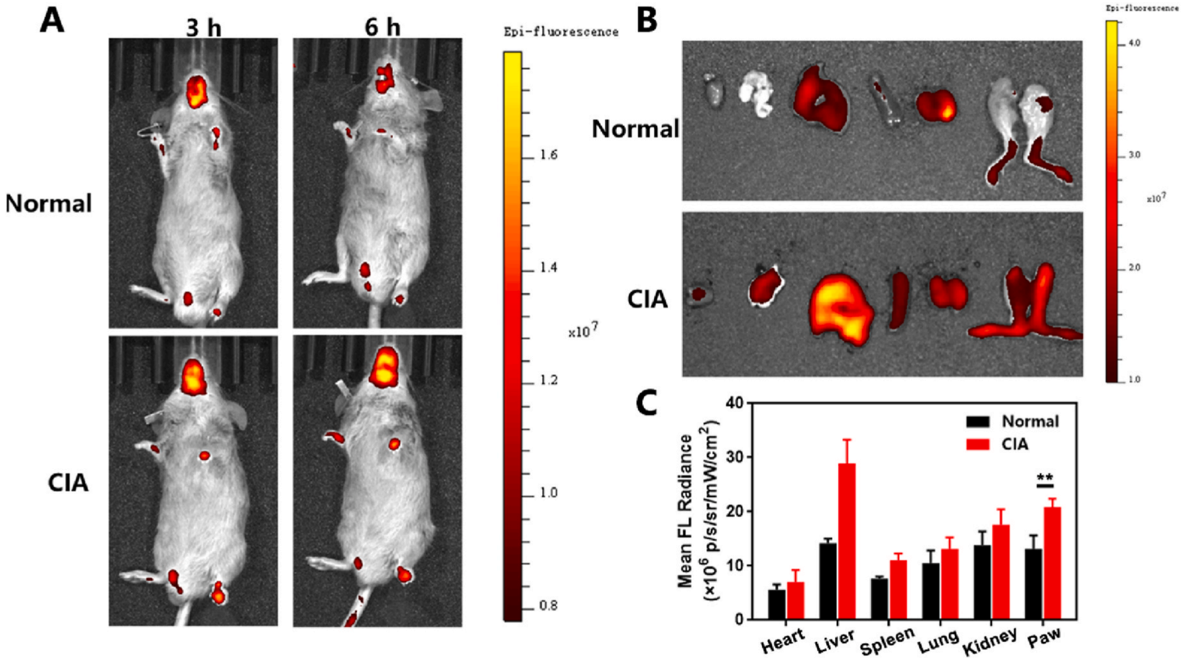

Fig. 5. *In vivo* biodistribution of TPH/CH MN applied in CIA mice. (A) IVIS fluorescent images of normal mice and CIA mice treated by TOTO-3 labeled TPH/CH MN at 3 and 6 h. (B) Fluorescence images of the major organs collected from normal and CIA mice after TOTO-3 labeled TPH/CH MN application post 6 h. (C) Quantitative fluorescence analysis for the major organs and paws. Data are shown as the mean ± SD (n = 3). $*p < 0.05$, $**p < 0.01$, $***p < 0.001$.

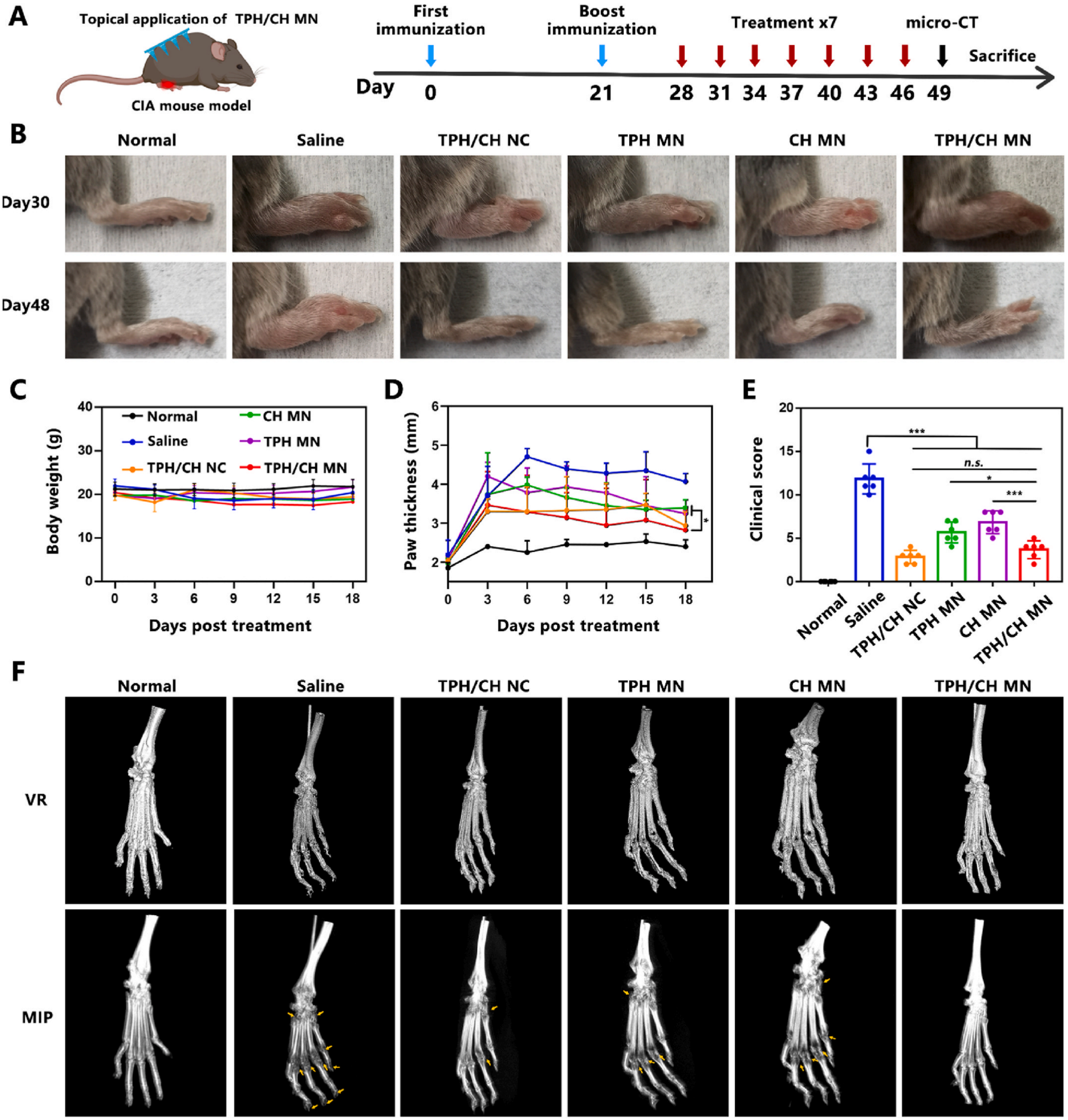

Fig. 6. Inhibitory effect of TPH/CH MN on arthritic progression in CIA mice. (A) Schematic illustration of the treatment for CIA mice by TPH/CH MN. (B) Representative hind paw images in normal, saline, TPH/CH NCs, TPH MN, CH MN and TPH/CH MN groups at day 30 and day 48. (C) Body weight change *vs* time in different groups. (D) Paw thickness of mice in normal, saline, TPH/CH NCs, TPH MN, CH MN and TPH/CH MN groups. (E) Clinical scores of mice at the end of the therapy. (F) Micro-CT analysis of the hind paw of mice after treatments. Data are shown as the mean ± SD (n = 6, *$p < 0.05$, **$p < 0.01$, and ***$p < 0.001$).

inflammatory cell infiltration. TPH/CH treatment displayed more efficient joint and synovial recovery with minimal pathologic features such as synovial hyperplasia, inflammatory cell infiltration and pannus invasion. In addition, the results of safranin O that stains the glycosaminoglycans of cartilage reveled evident cartilage damage in saline-treated CIA mice (Fig. 7B). CH MN couldn't effectively reduce cartilage damage, which indicated the limited cartilage protection effect of merely anti-inflammation of Cel. Instead, the cartilage of mice treated by TPH MN and TPH/CH MN remained intact structure and component similar as the normal mice, suggesting the cartilage preservation potential by promoting RA FLS depletion. Similar cartilage preservation results could be observed in toluidine blue (TB) staining (Fig. 7C). The serum levels of pro-inflammatory cytokines (TNF-α, IL-6 and IL-1β) were assessed by enzyme-linked immunosorbent assay (ELISA) to evaluate the potential systemic response and therapeutic efficacy of TPH/CH MN (Fig. 7D–F). As expected, the concentrations of TNF-α, IL-6 and IL-1β in serum were

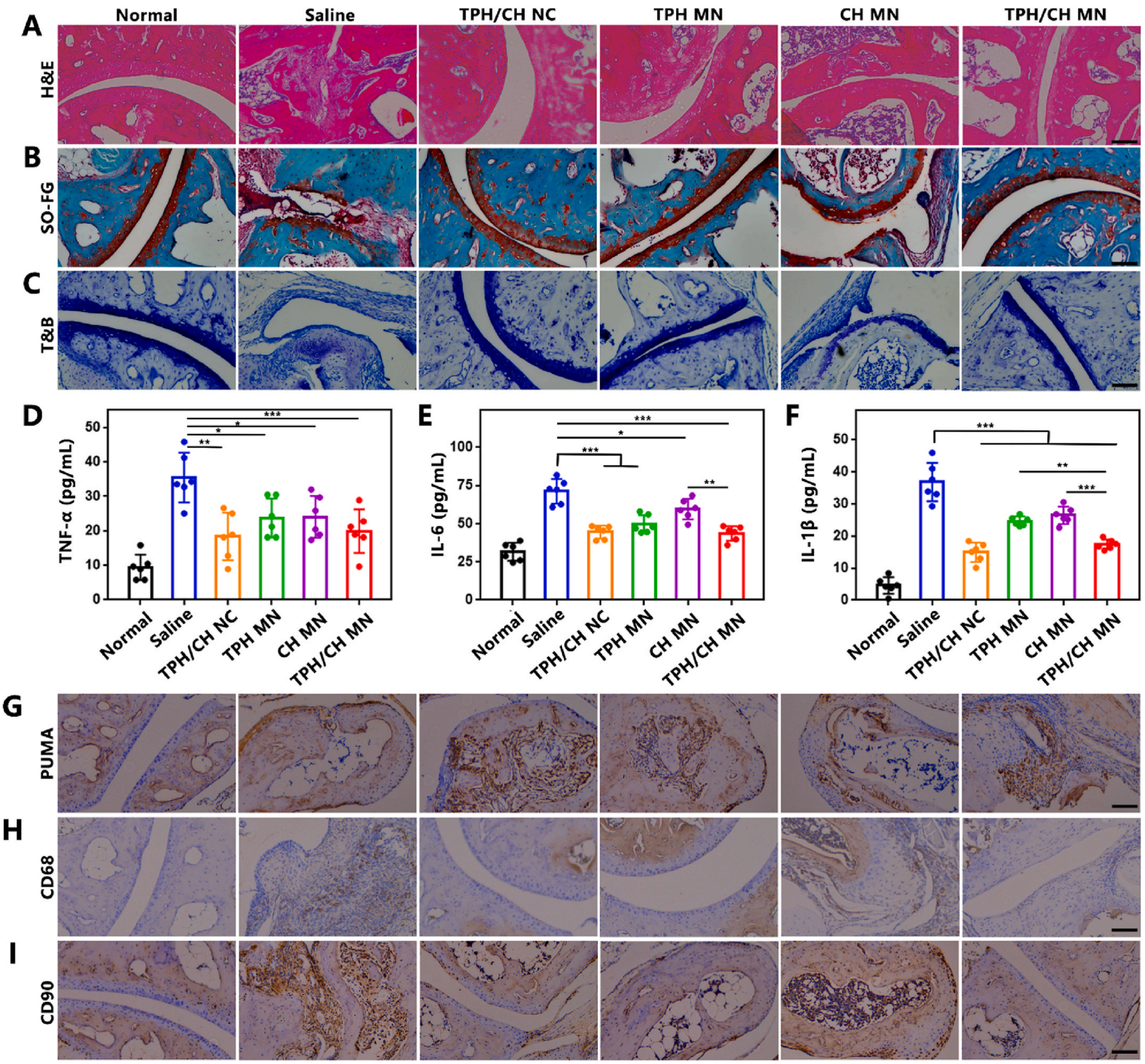

Fig. 7. The effect of TPH/CH MN on relieving arthritic inflammation and cartilage damage. Histological analysis with H&E (A), safranin-O staining (B) and TB staining (C) of joint tissues extracted from mice in normal, saline, TPH/CH NCs, TPH MN, CH MN and TPH/CH MN groups. Scale bar: 100 μm. (D–F) *In vivo* serum cytokines evaluation comprising of TNF-α (D), IL-6 (E) and IL-1β (F), n = 6. (G–I) Levels of PUMA (G), CD68 (H) and CD90 (I) in the arthritic joints of CIA mice evaluated by immunochemistry. Scale bar: 100 μm. Data are shown as the mean ± SD, $^*p < 0.05$, $^{**}p < 0.01$, and $^{***}p < 0.001$.

significantly increased in saline-treated CIA mice compared with normal mice. CH MN administration significantly decreased three pro-inflammatory cytokine levels owing to the anti-inflammatory effect of Cel. TPH MN also partially lowered pro-inflammatory cytokine levels, possibly attributed to the RA FLS depletion decreasing the secretion of pro-inflammatory cytokines [58]. TPH/CH MN group exhibited the lowest level of pro-inflammatory cytokines, which could be the outcome of simultaneous regulating these two RA-related cell types including RA FLS and macrophages.

To confirm the PUMA upregulation effect induced by TPH, we performed the immunohistochemical staining of PUMA protein in the joints. The numbers of PUMA-positive cells in ankle joints treated by TPH MN and TPH/CH MN surpassed those in saline and CH MN group, which indicated the transfection capacity of TPH (Fig. 7G). Immunohistochemical staining of macrophage-specific biomarker (CD68) and FLS-specific biomarker (CD90) were carried out to investigate the abundance of macrophages and FLS in inflamed joints, respectively [58,59]. Compared with saline group, CH MN, TPH MN and CH/TPH MN could both reduce the quantity of CD68 positive macrophages existing in the synovium (Fig. 7H). The effect of decreasing inflammatory macrophages through inducing FLS apoptosis could be attributed to the fact that FLS aggravates synovial inflammation by producing cytokines to recruit and activate immune cells [60]. In addition, TPH MN and CH/TPH MN treatment remarkably reduced the number of FLS while CH MN group didn't reveal obvious FLS decrease (Fig. 7I), which suggested FLS depletion effect *via* PUMA upregulation. These results implied that TPH/CH MN effectively decreased the abundance of both inflammatory FLS and macrophages in CIA mice.

4. Conclusion

In conclusion, we reported a dissolvable microneedle loaded with dual HSA-contained nanocomplexes to realize both apoptosis induction of RA FLS and inflammatory inhibition of macrophages based on gene-chemo combined therapy. The fabricated TPH/CH MN exhibited the following features: (1) MN-mediated transdermal delivery of dual nanodrug delivery systems to allow subsequent joint accumulation based on ELVIS effect and HSA-assisted biomimetic delivery; (2) the constructed thioketal-crosslinked fluorinated polyethyleneimine 1.8 K (^{TK}PF) exhibited superior transfection efficiency of PUMA plasmid in RA FLS; (3) Cel-loaded HSA nanocomplex with pH-responsive release property could suppress the LPS-stimulated inflammatory responses of RAW264.7 macrophages. (4) Simultaneously regulating RA FLS and macrophages to restore synovial homeostasis could effectively attenuate CIA symptoms, reduce inflammation infiltration, as well as relieve cartilage damage and bone erosion. Moreover, the proof-of-concept trials provided a versatile and user-friendly platform to treat chronic or autoimmune diseases through multiple targeting therapy.

Declaration of competing interest

The authors declare no conflicts of interest.

Ethics approval and consent to participate

All animal experiments were conducted in accordance with the regulations approved by the Animal Care and Use Committee of Zunyi Medical University (Zhuhai campus, permit no. ZHSC-2-2023-043).

CRediT authorship contribution statement

Peng Hua: Writing – original draft, Visualization, Validation, Methodology, Investigation, Formal analysis, Data curation, Conceptualization. **Ruifeng Liang:** Methodology, Investigation. **Suleixin Yang:** Methodology, Investigation. **Yanbei Tu:** Writing – review & editing. **Meiwan Chen:** Writing – review & editing, Supervision, Resources, Project administration, Funding acquisition, Conceptualization.

Acknowledgments

This study was supported by the Science and Technology Development Fund, Macau SAR (File no. 0124/2019/A3), and the University of Macau (File no. MYRG2022-00203-ICMS, MYRG-GRG2023-00134-ICMS-UMDF).

Appendix A. Supplementary data

Supplementary data to this article can be found online at https://doi.org/10.1016/j.bioactmat.2024.02.030.

References

[1] J.S. Smolen, D. Aletaha, A. Barton, G.R. Burmester, P. Emery, G.S. Firestein, A. Kavanaugh, I.B. McInnes, D.H. Solomon, V. Strand, K. Yamamoto, Rheumatoid arthritis, Nat. Rev. Dis. Prim. 4 (2018) 18001.

[2] D.L. Scott, F. Wolfe, T.W. Huizinga, Rheumatoid arthritis, Lancet (London, England) 376 (2010) 1094–1108.

[3] P.H. Hsieh, O. Wu, C. Geue, E. McIntosh, I.B. McInnes, S. Siebert, Economic burden of rheumatoid arthritis: a systematic review of literature in biologic era, Ann. Rheum. Dis. 79 (2020) 771–777.

[4] K. Redlich, J.S. Smolen, Inflammatory bone loss: pathogenesis and therapeutic intervention, Nat. Rev. Drug Discov. 11 (2012) 234–250.

[5] A.P. Croft, J. Campos, K. Jansen, J.D. Turner, J. Marshall, M. Attar, L. Savary, C. Wehmeyer, A.J. Naylor, S. Kemble, J. Begum, K. Dürholz, H. Perlman, F. Barone, H.M. McGettrick, D.T. Fearon, K. Wei, S. Raychaudhuri, I. Korsunsky, M. B. Brenner, M. Coles, S.N. Sansom, A. Filer, C.D. Buckley, Distinct fibroblast subsets drive inflammation and damage in arthritis, Nature 570 (2019) 246–251.

[6] G. Nygaard, G.S. Firestein, Restoring synovial homeostasis in rheumatoid arthritis by targeting fibroblast-like synoviocytes, Nat. Rev. Rheumatol. 16 (2020) 316–333.

[7] J. Wu, Z. Feng, L. Chen, Y. Li, H. Bian, J. Geng, Z.-H. Zheng, X. Fu, Z. Pei, Y. Qin, L. Yang, Y. Zhao, K. Wang, R. Chen, Q. He, G. Nan, X. Jiang, Z.-N. Chen, P. Zhu, TNF antagonist sensitizes synovial fibroblasts to ferroptotic cell death in collagen-induced arthritis mouse models, Nat. Commun. 13 (2022) 676.

[8] S. Alivernini, G.S. Firestein, I.B. McInnes, The pathogenesis of rheumatoid arthritis, Immunity 55 (2022) 2255–2270.

[9] Y. Wen, M. Zhang, Y. Yao, Y. Gao, X. Zhang, Y. Lin, X. Cai, Biological regulation on synovial fibroblast and the treatment of rheumatoid arthritis by nobiletin-loaded tetrahedral framework nucleic acids cargo tank, Chin. Chem. Lett. 34 (2023) 107549.

[10] M.F. Bustamante, P.G. Oliveira, R. Garcia-Carbonell, A.P. Croft, J.M. Smith, R. L. Serrano, E. Sanchez-Lopez, X. Liu, T. Kisseleva, N. Hay, C.D. Buckley, G. S. Firestein, A.N. Murphy, S. Miyamoto, M. Guma, Hexokinase 2 as a novel selective metabolic target for rheumatoid arthritis, Ann. Rheum. Dis. 77 (2018) 1636–1643.

[11] M.N.D. Svensson, M. Zoccheddu, S. Yang, G. Nygaard, C. Secchi, K.M. Doody, K. Slowikowski, F. Mizoguchi, F. Humby, R. Hands, E. Santelli, C. Sacchetti, K. Wakabayashi, D.J. Wu, C. Barback, R. Ai, W. Wang, G.P. Sims, P. Mydel, T. Kasama, D.L. Boyle, F. Galimi, D. Vera, M.L. Tremblay, S. Raychaudhuri, M.B. Brenner, G.S. Firestein, C. Pitzalis, A.-K.H. Ekwall, S.M. Stanford, N. Bottini, Synoviocyte-targeted therapy synergizes with TNF inhibition in arthritis reversal, Sci. Adv. 6, eaba4353.

[12] K.M. Doody, S.M. Stanford, C. Sacchetti, M.N.D. Svensson, C.H. Coles, N. Mitakidis, W.B. Kiosses, B. Bartok, C. Fos, E. Cory, R.L. Sah, R. Liu-Bryan, D.L. Boyle, H. A. Arnett, T. Mustelin, M. Corr, J.D. Esko, M.L. Tremblay, G.S. Firestein, A. R. Aricescu, N. Bottini, Targeting phosphatase-dependent proteoglycan switch for rheumatoid arthritis therapy, Sci. Transl. Med. 7 (2015), 288ra76-288ra76.

[13] H.-S. Cha, E.-K. Bae, J.K. Ahn, J. Lee, K.-S. Ahn, E.-M. Koh, Slug suppression induces apoptosis via Puma transactivation in rheumatoid arthritis fibroblast-like synoviocytes treated with hydrogen peroxide, Exp. Mol. Med. 42 (2010) 428–436.

[14] S.-S. Hong, H. Marotte, G. Courbon, G.S. Firestein, P. Boulanger, P. Miossec, PUMA gene delivery to synoviocytes reduces inflammation and degeneration of arthritic joints, Nat. Commun. 8 (2017) 146.

[15] H.-S. Cha, S. Rosengren, D.L. Boyle, G.S. Firestein, PUMA regulation and proapoptotic effects in fibroblast-like synoviocytes, Arthritis Rheum. 54 (2006) 587–592.

[16] H. Yin, R.L. Kanasty, A.A. Eltoukhy, A.J. Vegas, J.R. Dorkin, D.G. Anderson, Non-viral vectors for gene-based therapy, Nat. Rev. Genet. 15 (2014) 541–555.

[17] D.T. Ewart, E.J. Peterson, C.J. Steer, Gene editing for inflammatory disorders, Ann. Rheum. Dis. 78 (2019) 6–15.

[18] Z. Xu, Q. Wang, H. Zhong, Y. Jiang, X. Shi, B. Yuan, N. Yu, S. Zhang, X. Yuan, S. Guo, Y. Yang, Carrier strategies boost the application of CRISPR/Cas system in gene therapy, Explorations 2 (2022) 20210081.

[19] P. Hua, D. Yang, R. Chen, P. Qiu, M. Chen, ROS responsive polyethylenimine-based fluorinated polymers for enhanced transfection efficiency and lower cytotoxicity, Biomolecules and Biomedicine 22 (2022) 593–607.

[20] S. Yang, K.H. Wong, P. Hua, C. He, H. Yu, D. Shao, Z. Shi, M. Chen, ROS-responsive fluorinated polyethyleneimine vector to co-deliver shMTHFD2 and shGPX4 plasmids induces ferroptosis and apoptosis for cancer therapy, Acta Biomater. 140 (2022) 492–505.

[21] S. Kemble, A.P. Croft, Critical role of synovial tissue-resident macrophage and fibroblast subsets in the persistence of joint inflammation, Front. Immunol. 12 (2021) 715894.

[22] J.S. Smolen, D. Aletaha, I.B. McInnes, Rheumatoid arthritis, Lancet 388 (2016) 2023–2038.

[23] Y. Lin, O. Yi, M. Hu, S. Hu, Z. Su, J. Liao, W. Wang, S. Wang, L. Liu, B. Liu, X. Cai, Multifunctional nanoparticles of sinomenine hydrochloride for treat-to-target therapy of rheumatoid arthritis via modulation of proinflammatory cytokines, J. Contr. Release 348 (2022) 42–56.

[24] D.N. Huang, F.F. Wu, A.H. Zhang, H. Sun, X.J. Wang, Efficacy of berberine in treatment of rheumatoid arthritis: from multiple targets to therapeutic potential, Pharmacol. Res. 169 (2021) 105667.

[25] M. Jing, J. Yang, L. Zhang, J. Liu, S. Xu, M. Wang, L. Zhang, Y. Sun, W. Yan, G. Hou, C. Wang, W. Xin, Celastrol inhibits rheumatoid arthritis through the ROS-NF-κB-NLRP3 inflammasome axis, Int. Immunopharm. 98 (2021) 107879.

[26] L. Zhang, W. Meng, X. Chen, L. Wu, M. Chen, Z. Zhou, Y. Chen, L. Yuan, M. Chen, J. Chen, P. Shui, Multifunctional nanoplatform for mild microwave-enhanced thermal, antioxidative, and chemotherapeutic treatment of rheumatoid arthritis, ACS Appl. Mater. Interfaces 15 (2023) 10341–10355.

[27] L. An, Z. Li, L. Shi, L. Wang, Y. Wang, L. Jin, X. Shuai, J. Li, Inflammation-targeted celastrol nanodrug attenuates collagen-induced arthritis through NF-κB and Notch 1 pathways, Nano Lett. 20 (2020) 7728–7736.

[28] T. Zhang, C. Ma, Z. Zhang, H. Zhang, H. Hu, NF-κB signaling in inflammation and cancer, MedComm 2 (2021) 618–653.

[29] S. Gorantla, U. Batra, E.R. Puppala, T. Waghule, V.G.M. Naidu, G. Singhvi, Emerging trends in microneedle-based drug delivery strategies for the treatment of rheumatoid arthritis, Expet Opin. Drug Deliv. 19 (2022) 395–407.

[30] Y. Zhang, Y. Xu, H. Kong, J. Zhang, H.F. Chan, J. Wang, D. Shao, Y. Tao, M. Li, Microneedle system for tissue engineering and regenerative medicine, Explorations 3 (2023) 20210170.

[31] Y. Xu, M. Zhao, J. Cao, T. Fang, J. Zhang, Y. Zhen, F. Wu, X. Yu, Y. Liu, J. Li, D. Wang, Applications and recent advances in transdermal drug delivery systems for the treatment of rheumatoid arthritis, Acta Pharm. Sin. B 13 (2023) 4417–4441.

[32] T. Wan, Q. Pan, Y. Ping, Microneedle-assisted genome editing: a transdermal strategy of targeting NLRP3 by CRISPR-Cas9 for synergistic therapy of inflammatory skin disorders, Sci. Adv. 7, eabe2888.
[33] Z. Wang, Z. Yang, J. Jiang, Z. Shi, Y. Mao, N. Qin, T.H. Tao, Silk microneedle patch capable of on-demand multidrug delivery to the brain for glioblastoma treatment, Adv. Mater. 34 (2022) 2106606.
[34] Z. Wang, J. Wang, H. Li, J. Yu, G. Chen, A.R. Kahkoska, V. Wu, Y. Zeng, D. Wen, J. R. Miedema, J.B. Buse, Z. Gu, Dual self-regulated delivery of insulin and glucagon by a hybrid patch, Proc. Natl. Acad. Sci. USA 117 (2020) 29512–29517.
[35] L. Liu, F. Hu, H. Wang, X. Wu, A.S. Eltahan, S. Stanford, N. Bottini, H. Xiao, M. Bottini, W. Guo, X.J. Liang, Secreted protein acidic and rich in cysteine mediated biomimetic delivery of methotrexate by albumin-based nanomedicines for rheumatoid arthritis therapy, ACS Nano 13 (2019) 5036–5048.
[36] N. Fan, J. Zhao, W. Zhao, X. Zhang, Q. Song, Y. Shen, H.C. Shum, Y. Wang, J. Rong, Celastrol-loaded lactosylated albumin nanoparticles attenuate hepatic steatosis in non-alcoholic fatty liver disease, J. Contr. Release 347 (2022) 44–54.
[37] P. Hua, D. Jiang, Z. Guo, H. Tian, X. Chen, M. Chen, Amplified cancer immunotherapy of PD-L1 blockade by sequential tumor microenvironment reshaping and DC maturation, Chem. Eng. J. 453 (2023) 139795.
[38] X. Zhang, X. Xu, X. Wang, Y. Lin, Y. Zheng, W. Xu, J. Liu, W. Xu, Hepatoma-targeting and reactive oxygen species-responsive chitosan-based polymeric micelles for delivery of celastrol, Carbohydr. Polym. 303 (2023) 120439.
[39] H. Du, P. Liu, J. Zhu, J. Lan, Y. Li, L. Zhang, J. Zhu, J. Tao, Hyaluronic acid-based dissolving microneedle patch loaded with methotrexate for improved treatment of psoriasis, ACS Appl. Mater. Interfaces 11 (2019) 43588–43598.
[40] Q. Zhang, D. Dehaini, Y. Zhang, J. Zhou, X. Chen, L. Zhang, R.H. Fang, W. Gao, L. Zhang, Neutrophil membrane-coated nanoparticles inhibit synovial inflammation and alleviate joint damage in inflammatory arthritis, Nat. Nanotechnol. 13 (2018) 1182–1190.
[41] D.D. Brand, K.A. Latham, E.F. Rosloniec, Collagen-induced arthritis, Nat. Protoc. 2 (2007) 1269–1275.
[42] J. Dang, H. Ye, Y. Li, Q. Liang, X. Li, L. Yin, Multivalency-assisted membrane-penetrating siRNA delivery sensitizes photothermal ablation via inhibition of tumor glycolysis metabolism, Biomaterials 223 (2019) 119463.
[43] J. Shen, H. Gao, L. Chen, Y. Jiang, S. Li, Y. Chao, N. Liu, Y. Wang, T. Wei, Y. Liu, J. Li, M. Chen, J. Zhu, J. Liang, X. Zhou, X. Zhang, P. Gu, Q. Chen, Z. Liu, Eyedrop-based macromolecular ophthalmic drug delivery for ocular fundus disease treatment, Sci. Adv. 9, eabq3104.
[44] M.M. Alam, H.S. Han, S. Sung, J.H. Kang, K.H. Sa, H. Al Faruque, J. Hong, E. J. Nam, I.S. Kim, J.H. Park, Y.M. Kang, Endogenous inspired biomineral-installed hyaluronan nanoparticles as pH-responsive carrier of methotrexate for rheumatoid arthritis, J. Contr. Release 252 (2017) 62–72.
[45] Y. Liu, J. Jin, H. Xu, C. Wang, Y. Yang, Y. Zhao, H. Han, T. Hou, G. Yang, L. Zhang, Y. Wang, W. Zhang, Q. Liang, Construction of a pH-responsive, ultralow-dose triptolide nanomedicine for safe rheumatoid arthritis therapy, Acta Biomater. 121 (2021) 541–553.
[46] Y. Li, G. He, L.-H. Fu, M.R. Younis, T. He, Y. Chen, J. Lin, Z. Li, P. Huang, A microneedle patch with self-oxygenation and glutathione depletion for repeatable photodynamic therapy, ACS Nano 16 (2022) 17298–17312.
[47] S. Zhang, Y. Liu, W. Jing, Q. Chai, C. Tang, Z. Li, Z. Man, C. Chen, J. Zhang, P. Sun, R. Zhang, Z. Yang, M. Han, Y. Wang, X. Wei, J. Li, W. Li, M. Abdalla, G. Yu, B. Shi, Y. Zhang, K. Zhao, X. Jiang, Remodeling articular immune homeostasis with an efferocytosis-informed nanoimitator mitigates rheumatoid arthritis in mice, Nat. Commun. 14 (2023) 817.
[48] C. Loh, S.H. Park, A. Lee, R. Yuan, L.B. Ivashkiv, G.D. Kalliolias, TNF-induced inflammatory genes escape repression in fibroblast-like synoviocytes: transcriptomic and epigenomic analysis, Ann. Rheum. Dis. 78 (2019) 1205–1214.
[49] M. Wang, H. Liu, L. Li, Y. Cheng, A fluorinated dendrimer achieves excellent gene transfection efficacy at extremely low nitrogen to phosphorus ratios, Nat. Commun. 5 (2014) 3053.
[50] T. Zhang, Y. Huang, X. Ma, N. Gong, X. Liu, L. Liu, X. Ye, B. Hu, C. Li, J.H. Tian, A. Magrini, J. Zhang, W. Guo, J.F. Xing, M. Bottini, X.J. Liang, Fluorinated oligoethylenimine nanoassemblies for efficient siRNA-mediated gene silencing in serum-containing media by effective endosomal escape, Nano Lett. 18 (2018) 6301–6311.
[51] L. Liu, F. Hu, H. Wang, X. Wu, A.S. Eltahan, S. Stanford, N. Bottini, H. Xiao, M. Bottini, W. Guo, X.-J. Liang, Secreted protein acidic and rich in cysteine mediated biomimetic delivery of methotrexate by albumin-based nanomedicines for rheumatoid arthritis therapy, ACS Nano 13 (2019) 5036–5048.
[52] I.M.S. Degors, C. Wang, Z.U. Rehman, I.S. Zuhorn, Carriers break barriers in drug delivery: endocytosis and endosomal escape of gene delivery vectors, Accounts Chem. Res. 52 (2019) 1750–1760.
[53] J. Yang, L. Song, M. Shen, X. Gou, L. Bai, L. Wang, W. Zhang, Q. Wu, C. Gong, Hierarchically responsive tumor-microenvironment-activated nano-artificial virus for precise exogenous and endogenous apoptosis coactivation, Adv. Funct. Mater. 31 (2021) 2104423.
[54] P.-F. Cui, L.-Y. Qi, Y. Wang, R.-Y. Yu, Y.-J. He, L. Xing, H.-L. Jiang, Dex-Aco coating simultaneously increase the biocompatibility and transfection efficiency of cationic polymeric gene vectors, J. Contr. Release 303 (2019) 253–262.
[55] R. Robb, J.C. Kuo, Y. Liu, S. Corrales-Guerrero, T. Cui, A. Hegazi, G. Nagy, R.J. Lee, T.M. Williams, A novel protein-drug conjugate, SSH20, demonstrates significant efficacy in caveolin-1-expressing tumors, Molecular therapy oncolytics 22 (2021) 555–564.
[56] X. Yu, X. Meng, M. Xu, X. Zhang, Y. Zhang, G. Ding, S. Huang, A. Zhang, Z. Jia, Celastrol ameliorates cisplatin nephrotoxicity by inhibiting NF-κB and improving mitochondrial function, EBioMedicine 36 (2018) 266–280.
[57] R. Cornu, A. Béduneau, H. Martin, Influence of nanoparticles on liver tissue and hepatic functions: a review, Toxicology 430 (2020) 152344.
[58] F. Mizoguchi, K. Slowikowski, K. Wei, J.L. Marshall, D.A. Rao, S.K. Chang, H. N. Nguyen, E.H. Noss, J.D. Turner, B.E. Earp, P.E. Blazar, J. Wright, B.P. Simmons, L.T. Donlin, G.D. Kalliolias, S.M. Goodman, V.P. Bykerk, L.B. Ivashkiv, J. A. Lederer, N. Hacohen, P.A. Nigrovic, A. Filer, C.D. Buckley, S. Raychaudhuri, M. B. Brenner, Functionally distinct disease-associated fibroblast subsets in rheumatoid arthritis, Nat. Commun. 9 (2018) 789.
[59] M.J. Boumans, J.G. Houbiers, P. Verschueren, H. Ishikura, R. Westhovens, E. Brouwer, B. Rojkovich, S. Kelly, M. den Adel, J. Isaacs, H. Jacobs, J. Gomez-Reino, G.M. Holtkamp, A. Hastings, D.M. Gerlag, P.P. Tak, Safety, tolerability, pharmacokinetics, pharmacodynamics and efficacy of the monoclonal antibody ASK8007 blocking osteopontin in patients with rheumatoid arthritis: a randomised, placebo controlled, proof-of-concept study, Ann. Rheum. Dis. 71 (2012) 180–185.
[60] C. Carmona-Rivera, P.M. Carlucci, E. Moore, N. Lingampalli, H. Uchtenhagen, E. James, Y. Liu, K.L. Bicker, H. Wahamaa, V. Hoffmann, A.I. Catrina, P. R. Thompson, J.H. Buckner, W.H. Robinson, D.A. Fox, M.J. Kaplan, Synovial fibroblast-neutrophil interactions promote pathogenic adaptive immunity in rheumatoid arthritis, Science Immunology 2 (2017) eaag3358.